Measurement of tidal and residual currents and volume transport through the Qiongzhou Strait using coastal acoustic tomography

Xiao-Hua Zhu [a,b,*], Ze-Nan Zhu [b,a], Xinyu Guo [a,c], Yun-Long Ma [a], Xiaopeng Fan [a], Menghong Dong [a], Chuanzheng Zhang [a]

[a] State Key Laboratory of Satellite Ocean Environment Dynamics, Second Institute of Oceanography, State Oceanic Administration, Hangzhou 310012, China
[b] Ocean College, Zhejiang University, Hangzhou 310058, China
[c] Center for Marine Environmental Study, Ehime University, 2-5 Bunkyo-cho, Matsuyama 790-8577, Japan

ARTICLE INFO

ABSTRACT

Quantifying the tidal current and volume transport through the Qiongzhou Strait (QS) is vital to understanding the circulation in the northern South China Sea. To measure the tidal current in the strait, a 15-day coastal acoustic tomography (CAT) experiment was carried out at four acoustic stations in March 2013. The horizontal distributions of the tidal currents were calculated by inverse analysis of CAT data. The diurnal tidal current constituents were found to dominate: the ratio of the amplitudes O_1, K_1, M_2, S_2, and MSF was 1.00:0.60:0.47:0.21:0.11. The residual currents were found to flow westward in the northern QS and turn southward in the southern QS. The residual current velocities were larger in the northern area than in the southern area, with a maximum westward velocity of 12.4 cm s^{-1} in the northern QS. Volume transport estimated using the CAT data varied between -0.710 Sv and 0.859 Sv, with residual current transport of -0.044 Sv, where negative values indicate westward. We conducted a dynamic analysis of the observations made during the study, which suggested that tidal rectification and sea level difference between the two entrances of the QS are important in maintaining the residual current through the strait. This is the first estimation, from synchronous measurements, of major tidal current constituents, residual currents, and volume transport in this strait.

© 2015 Elsevier Ltd. All rights reserved.

1. Introduction

The Qiongzhou Strait (QS) is a channel and key point of water exchange between the northern South China Sea and the Beibu Gulf (Fig. 1a). Quantifying the tidal current and volume transport through the QS is vital to understanding the coastal circulation and mass balance in the northern South China Sea and the cyclonic circulation in the Beibu Gulf (Wang et al., 2010; Wu et al., 2008).

Analysis performed by Shi et al. (2002) of current meter data and tide gauge data from 1963 to 1999 revealed a westward residual current through the QS throughout the year. They also roughly estimated the corresponding volume transport: approximately 0.2–0.4 Sv in winter and spring, and approximately 0.1–0.2 Sv in summer and autumn. These results agree with the more recent current meter mooring data collected at several stations and at different times (Chen et al., 2006, 2007; Yan et al., 2008), repeat shipboard ADCP data (Zhu et al., 2014), drifting bottle data

(Yang et al., 2003; Bao et al., 2005), and numerical studies (Chen et al., 2009). However, synchronous data measurements to directly probe the spatial structure of the tidal and residual currents and the resulting volume transport through the strait have not yet been performed.

To observe tidal current structures and volume transport through the QS, bottom-mounted acoustic Doppler current profilers (ADCP), arrays of subsurface moored current meters, or repeat shipboard ADCP surveys would normally be utilized. However, in the QS, the heavy shipping traffic and fishery activity prohibit the deployment of mooring arrays. The QS is studded with fishing nets, which also makes shipboard ADCP surveys difficult at night. Thus, *in situ* point current data are insufficient to determine the complete structure of tidal and residual currents in the QS.

To measure the current in the QS, we carried out a 15-day experiment using coastal acoustic tomography (CAT) systems (Kaneko et al., 2005; Yamaguchi et al., 2005) that do not disturb shipping traffic, fisheries, or marine aquaculture. To the best of our knowledge, this study is the first synchronous measurement that separates the major tidal current constituents and residual current in the QS.

---

* Corresponding author at: State Key Laboratory of Satellite Ocean Environment Dynamics, Second Institute of Oceanography, State Oceanic Administration, Hangzhou 310012, China. Fax: +86 571 88839374.
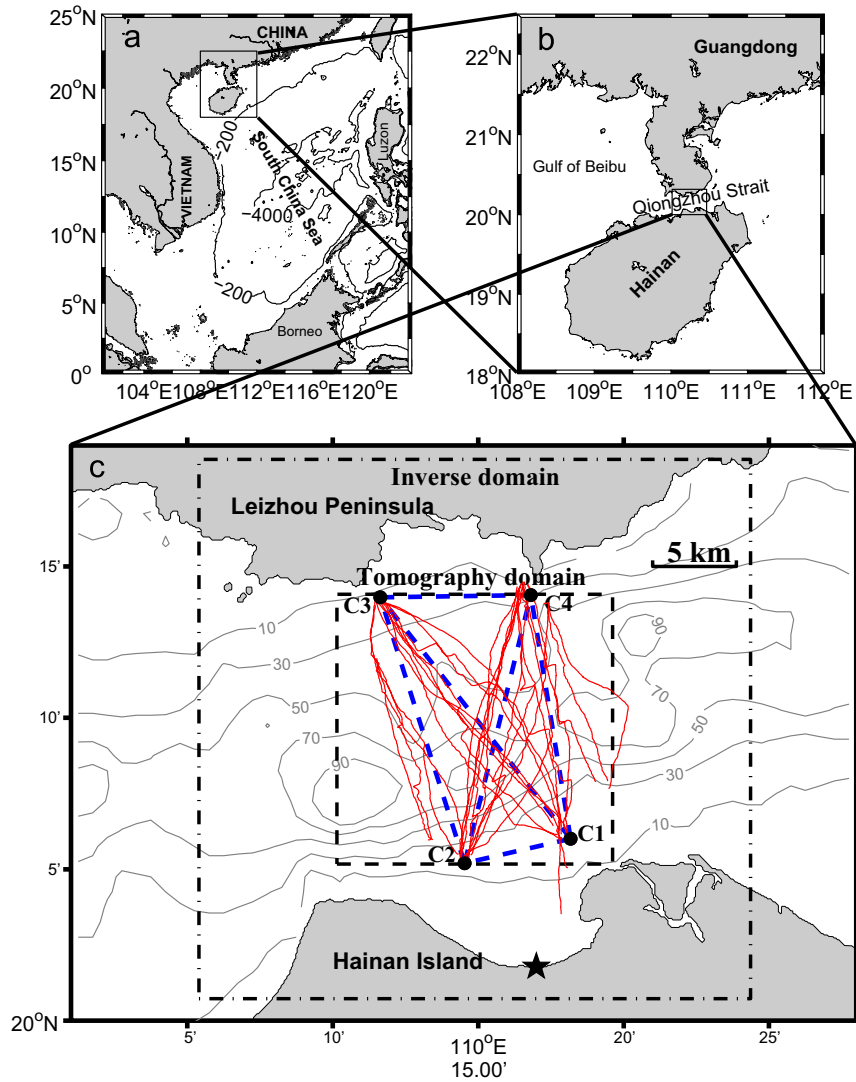E-mail address: xhzhu@sio.org.cn (X.-H. Zhu).

Fig. 1. Qiongzhou Strait and measurement sites. (a) Bathymetry of the South China Sea; (b) Location of the Qiongzhou Strait and Hainan Island, and (c) Bathymetry of the Qiongzhou Strait. The solid circles (C1–C4) indicate the positions of the CAT stations. The blue dashed lines indicate the sound transmission lines, the red lines indicate the shipboard ADCP tracks. The '★' indicates the position of the Haikou tidal gauge station. The interval of bathymetric contours is 20 m. (For interpretation of the references to color in this figure legend, the reader is referred to the web version of this article.)

2. Site and methods

Four CAT systems measured the currents in the QS (Fig. 1b) over a

15-day experiment period (March 17–April 1, 2013), which covered one fortnightly spring/neap tidal cycle (Fig. 2a). The CAT systems were set up using fishing ships anchored on both sides of the QS, at
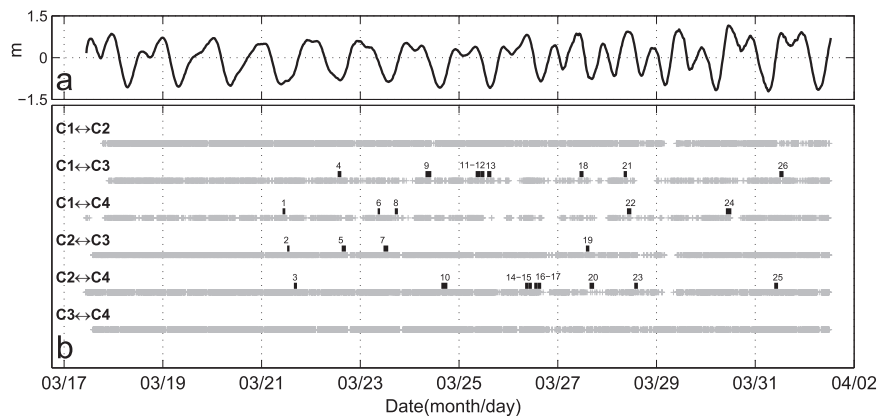

Fig. 2. Synchronized CAT and ADCP measurements. (a) The tidal level anomaly (black lines) observed at the Haikou tidal gauge station and (b) time periods of successful acquisition of reciprocal sound transmission (gray cross) between each station pair and the time schedule of the shipboard ADCP survey (black horizontal bar). The cruise number is indicated above the bars.

four stations numbered C1–C4, spanning an 11.5 km × 16.5 km area. The broadband transducers were suspended at a depth of about 7 m using a rope. During the CAT observation period, 26 along-line tracks of shipboard ADCP (RDI Workhorse 300-kHz) were performed across the QS (Figs. 1c and 2b).

An 11th order M sequence phase-modulated the transmitted 5 kHz sound used in this experiment, increasing the signal-to-noise ratio (SNR) of received signals by $20 \times \log \sqrt{2^{11} - 1} = 33.1$ dB. A Q-value of 3 cycles per digit set the frequency band-width to 5 kHz/$3 = 1.7$ kHz. The time resolution of multi-ray arrivals, defined as one-digit length of the M sequence, was 0.6 ms. One-period (2048 digits at 1.23 s) M sequences were transmitted every 5 min, simultaneously from all four stations. The clocks of the CAT systems at the four stations were synchronized by GPS with a very high timing accuracy of about ± 500 ns (Yamaguchi et al., 2005). Yamaguchi et al. (2005) gives detailed methods for various M sequence transmissions and resolution of acoustic signals from multiple stations. For current velocity measurements, positioning error due to anchored ship motion is negligible and does not affect the measured travel time difference of reciprocally transmitted sounds, which requires precise clock accuracy rather than the precise positioning accuracy (Munk et al., 1995).

Reciprocal sound transmissions were successfully carried out along the six lines spanning the four CAT stations. The successful sound transmission acquisition rates varied from 78% (between C1 and C4) to 97% (between C3 and C4), with a mean rate of 91% (Fig. 2b). The primary cause of data dropout in the QS was likely due to shipping wake generated bubbles or noises. The differential travel-time data were smoothed by a one-hour running mean, and then used in the inverse method to reconstruct the tidal currents.

The shipboard ADCP observations were performed in the daytime and synchronized with the CAT schedule inside the tomography domain (Figs. 1c and 2b). The ADCP was attached to the side of a wooden fishing ship using a stainless steel frame with its transducers maintained at a depth of 1 m. The ADCP sampled data at one ping per 2 s, with a bin number and bin length of 60 and 2 m, respectively. Under these conditions, the raw velocity error (standard deviation) for a single ping was less than 7.0 cm s^{-1} (Teledyne RD Instruments, 2013). The first ADCP bin depth and the blank distance from the bottom were approximately 3 m and 4 m, respectively. The velocity of the top 3 m and the bottom 4 m could not be measured directly and were determined by extrapolation, following the method proposed by Gordon (1989). We corrected compass biases, which were mainly due to the magnetic angle (Kaneko et al., 1992). After compass correction, velocity profiles obtained using bottom-tracking mode were averaged over a 100 m horizontal range (approximately 15 profiles mean) to produce a standard data set with a spatial interval of 100 m and an estimated error of $7.0/\sqrt{15} = 1.8$ cm s^{-1}. During the shipboard ADCP surveys, one conductivity, temperature, depth (CTD) cast was executed at the center of the tomography area to acquire parameters for use in the sound speed profile calculations for the ray simulation.

The inverse method (Park and Kaneko, 2001) reconstructed the horizontal distribution of depth averaged tidal currents from the differential travel-time data obtained from the reciprocal sound transmissions for all the CAT station pairs. The equation system relates the travel-time difference vector $\boldsymbol{y}$ to the unknown variable vector $\boldsymbol{x}$ as follows:

$$\boldsymbol{y} = \boldsymbol{E}\boldsymbol{x} + e, \tag{1}$$

where $\boldsymbol{y}$ is a 6th order column vector, corresponding to the total number of station pairs; $\boldsymbol{x}$ is a vector of the 20 unknown coefficients used in the Fourier function expansion of the stream function to estimate the current field; $\boldsymbol{E}$ is the 6×20 transform matrix, determined by the locations of the 4 CAT stations; e is the matrix

of observation errors. The maximum and minimum wavelengths (wavenumbers) in the Fourier expansion are 33 km ($\frac{6\pi}{33}$ km^{-1}) and 11 km ($\frac{2\pi}{33}$ km^{-1}), respectively. The objective function, with the tapered least squares method, is

$$\boldsymbol{J} = (\boldsymbol{y} - \boldsymbol{E}\boldsymbol{x})^T(\boldsymbol{y} - \boldsymbol{E}\boldsymbol{x}) + \alpha^2 \boldsymbol{x}^T \boldsymbol{x}, \tag{2}$$

where α is the weighting factor, which can be determined by the L-curve method. The expected solution is determined by minimizing $\boldsymbol{J}$.

The inverse domain is 33 km × 33 km (Fig. 1c), and the grid size for the data display is 2.8 km × 2.8 km, which is slightly smaller than the mean horizontal resolution of $\sqrt{A/N} = 4.4$ km, where $A = 115.6$ km^2 is the area of the tomography domain, and $N = 6$ is the ray number. Here we used a small grid size to interpolate the current vector from the stream function to show the fine structure of the measured current distribution. Apparently, the interpolation did not change the mean horizontal resolution of data.

3. Results

3.1. Ray simulation

The CTD cast at the center of the tomography area measured the water temperature to decrease from the surface to a depth of about 15 m and remain nearly constant from 15 to 80 m (Fig. 3a). A shallow water thermocline formed at a depth of approximately 10 m. As a result, a shallow water sound channel formed at a depth of around 7 m (Fig. 3a).

Ray patterns were obtained for two station pairs, C1–C3 and C2–C4 (Fig. 3b and c), by ray simulations. Ray simulations were performed using range-dependent bathymetry and a range-independent sound speed profile determined from the CTD data obtained during the CAT experiment (Fig. 3a). All rays were confined to the upper 30 m. The travelling sound formed direct rays along the shallow water sound channel axis or made three- or four-time subsurface bends below the direct rays. The values of the travel-time mean ± standard deviation for these rays are (11986.212 ± 0.044) ms for C1–C3 and (11064.161 ± 0.052) ms for C2–C4. The standard deviations of travel-time varied within a narrow range shorter than time resolution (0.6 ms). This indicates that the multi-path signals arrived at nearly the same time, making them indistinguishable by our instruments. All arrival rays within a one-digit length constructed a broad arrival peak, which determines the travel-time.

3.2. Along-strait current velocity and transport

The reciprocal sound transmission method (Munk et al., 1995) determines the section-averaged current velocity between two acoustic stations to be

$$u_m \approx \frac{c_m^2}{2L}\Delta\tau, \tag{3}$$

where c_m and u_m are the sound speed and current velocity averaged along the ray path, respectively; $\Delta\tau$ is the differential reciprocal travel time; and L the station-to-station distance.

Hourly mean section-averaged current velocity u_m along each transect (Fig. 4a–f) was estimated from $\Delta\tau$ using Eq. (1). $\bar{V}_{ADCP}$ denotes the shipboard ADCP velocities averaged over the entire section. u_m for each transect agrees well with $\bar{V}_{ADCP}$; the root-mean-squares differences (RMSD) between the two variables are 0.041 m s^{-1}, 0.036 m s^{-1}, 0.029 m s^{-1}, and 0.030 m s^{-1} for station pairs C1–C3, C1–C4, C2–C3, and C2–C4, respectively.

u_m for station pairs C1–C2, C1–C3, C2–C4, and C3–C4 change
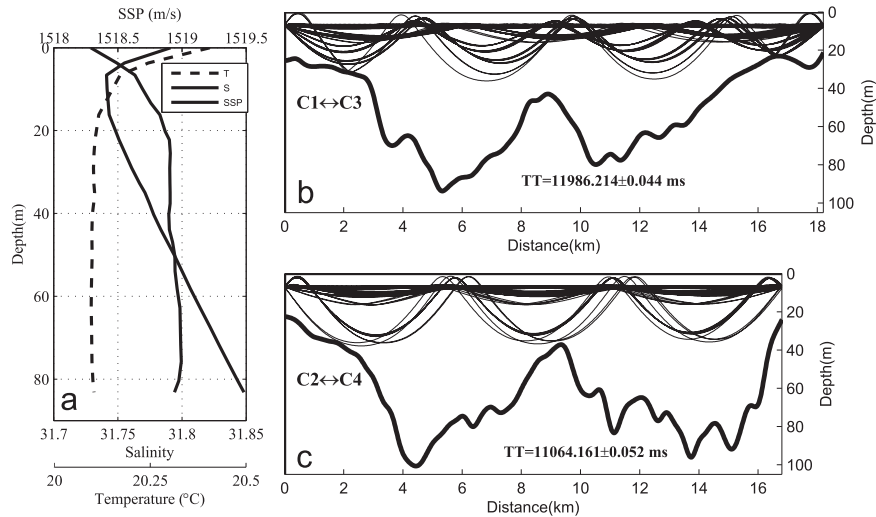
Fig. 3. (a) Water temperature and salinity profiles obtained in the centre of the QS, and their corresponding sound speed profiles (SSP). Ray patterns between (b) C1–C3 and (c) C2–C4 station pairs, simulated by the ray-tracing method using the range-averaged SSP profile. The (mean ± standard deviation) of the travel times are shown at the bottom of each panel.
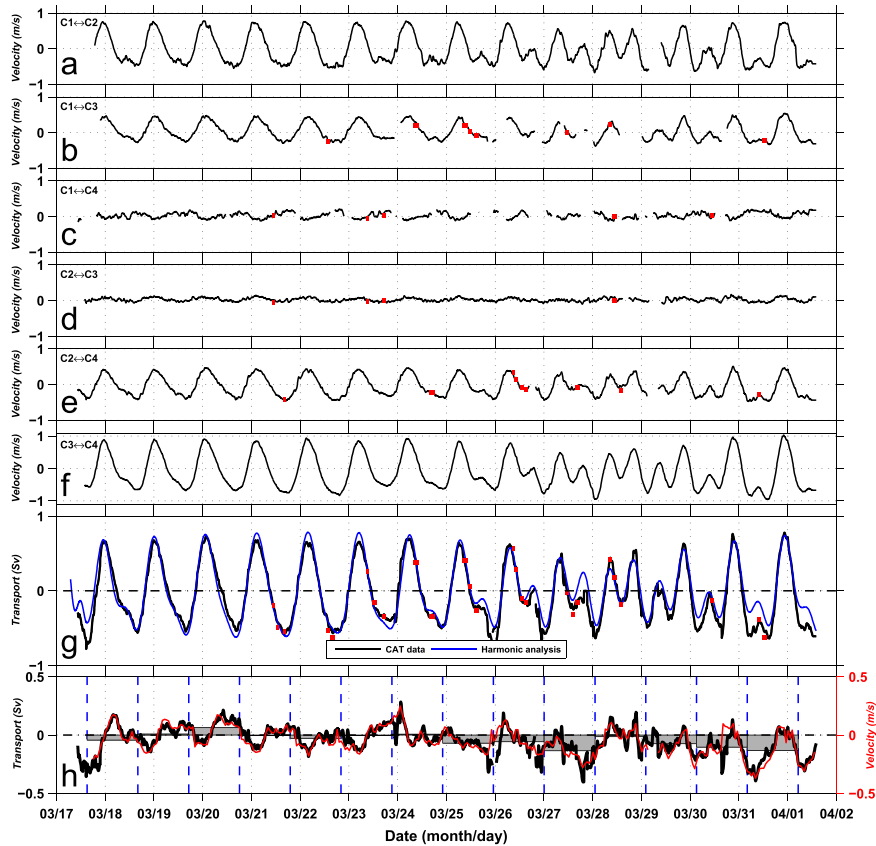

Fig. 4. Velocities along the sound transmission lines. (a)–(f) Time series of the section-averaged velocities along the sound transmission lines (C1–C2, C1–C3, C1–C4, C2–C3, C2–C4, and C3–C4), respectively; (g) the measured volume transport (Q_{CAT}, black line) and the value predicted based on harmonic constants (blue line), through the Qiongzhou Strait; (h) time series of the volume transport due to residual current (black line) and spatially mean residual current (red line) obtained by the inverse method. Shaded horizontal bars indicate mean volume transports in each diurnal tide period, separated by blue broken lines. Red rectangles in (b)–(e) and (g) indicate the section-averaged ADCP velocity and the volume transport given by ADCP velocity. Positive (negative) value indicates the eastward (westward) velocity or volume transport. (For interpretation of the references to color in this figure legend, the reader is referred to the web version of this article.)

with tidal phase. Diurnal tidal variation dominates the u_m from March 17 to 24, and semidiurnal tidal variation dominates from March 28 to 29 (Fig. 4a–f). Temporal variations of u_m are consistent with sea level anomalies (Fig. 2a). Station pair C3–C4 u_m reaches a maximum of about $\pm 1\,\mathrm{m\,s^{-1}}$ in the direction nearly parallel to the strait. The u_m of station pairs C1–C4 and C2–C3 are small

because these two sections are nearly perpendicular to the strait.

The u_m between the station pairs based on travel-time difference data are the mean velocities within the upper 30 m of the strait, because the acoustic rays only distributed in that upper layer (see Fig. 3b and c). Consequently, volume transport across the whole section cannot be estimated using u_m and the areas of
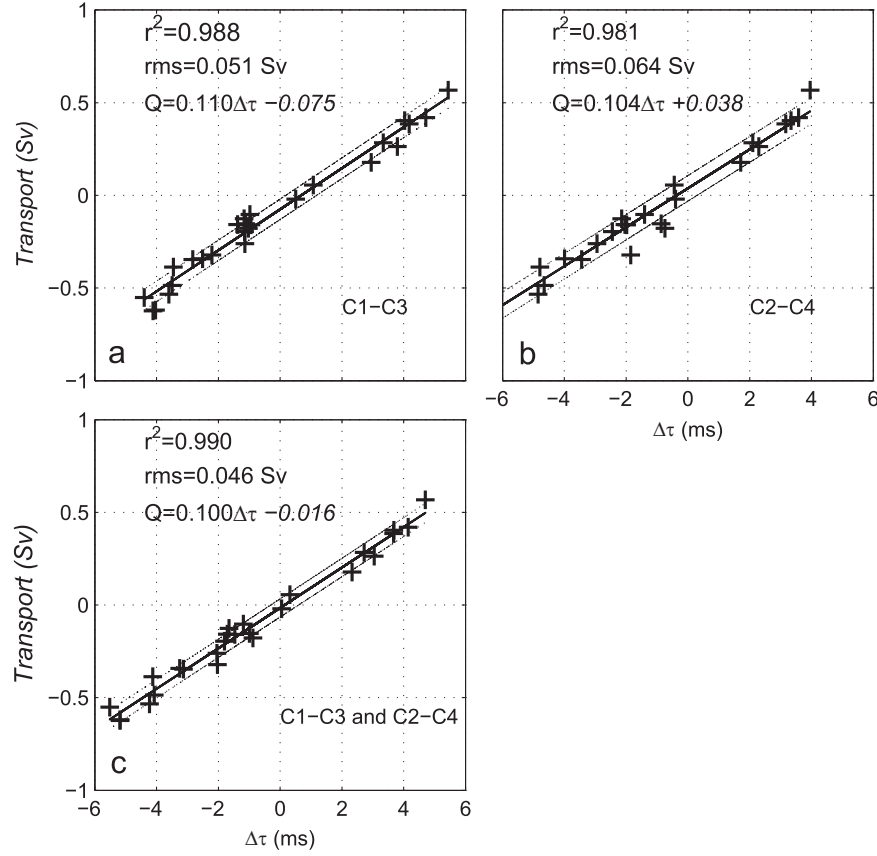
Fig. 5. The relationship between the differential travel time and the volume transport along the strait estimated from the ADCP data for station pairs. (a) C1–C3, (b) C2–C4, and (c) the mean of C1–C3 and C2–C4. The solid line indicates the regression line derived from the least squares method. The two gray broken lines indicate the range of standard deviation between the volume transport estimated from the ADCP data and the volume transport derived from differential travel time.

the vertical sections. On the other hand, volume transport along the strait can be estimated from the ADCP data (Q_{ADCP}) collected during the 26 cruises. However, the Q_{ADCP} data are available only during the time of the shipboard surveys. To acquire a time series of volume transport through the QS that allows for harmonic analysis, we established an empirical relationship between Q_{ADCP} and $\Delta\tau$, and applied this relation to all $\Delta\tau$ to obtain a $\Delta\tau$-based volume transport through the QS (Q_{CAT}).

Q_{ADCP} and $\Delta\tau$ are linearly related (Fig. 5) for station pairs C1–C3 (Fig. 5a), C2–C4 (Fig. 5b), and the mean of station pairs C1–C3 and C2–C4 (Fig. 5c), with correlation coefficients $r^2 = 0.988$, 0.981 and 0.990, and standard deviations of the differences between Q_{ADCP} and $\Delta\tau$ regression values of 0.051 Sv, 0.064 Sv, and 0.046 Sv, respectively. Therefore, the empirical formulae that relate $\Delta\tau$ to volume transport are

$$Q_{CAT} = 0.110 \times \Delta\tau_{C_1-C_3} - 0.075, \tag{4}$$

$$Q_{CAT} = 0.104 \times \Delta\tau_{C_2-C_4} + 0.038, \tag{5}$$

$$Q_{CAT} = 0.100 \times \Delta\tau_{mean} - 0.016, \tag{6}$$

where Q_{CAT} is the volume transport estimated from a $\Delta\tau$; and $\Delta\tau_{C_1-C_3}$, $\Delta\tau_{C_2-C_4}$ and $\Delta\tau_{mean}$ are the differential travel-times for station pairs C1–C3, C2C1–C4 and the mean differential travel time for station pairs C1–C3 and C2–C4, respectively. Since Eq. (6) gives the best results among the three equations, we prefer to use the mean differential travel time to estimate the Q_{CAT}; when the differential travel-time data for only one station pair of C1–C3 or C2–C4 are available, we use either Eqs. (4) or (5) to estimate Q_{CAT}.

As expected, Q_{CAT} agreed well with Q_{ADCP}, with a 0.045 Sv RMSD

(Fig. 4g). Consequently, the empirical formulae Eqs. (4)–(6) accurately estimated the volume transport through the QS with $\Delta\tau$ for the entire experiment period.

Q_{CAT} varied temporally with tide (Fig. 4g). Its value ranged from -0.710 to 0.859 Sv, with -0.044 Sv mean residual volume transport. Time dependent volume transport due to residual current is defined as the difference between the volume transport measurement (black line in Fig. 4g) and prediction (blue line in Fig. 4g), estimated by a tidal harmonic analysis using T_TIDE Matlab software (Pawlowicz et al., 2002). This transport also varied with diurnal tide (Fig. 4h). The mean volume transport of subtidal current averaged in each diurnal tide period (gray bars in Fig. 4h) was small when the diurnal tide was dominant (March 17–24) but large when the semidiurnal tide increased (after March 25).

3.3. Tidal current and residual current structures

As introduced in Section 2, the inverse method applied to CAT data (Park and Kaneko, 2001; Kaneko et al., 2005; Yamaguchi et al., 2005) gave the depth-averaged current (eastward and northward components) at the given grid points (Fig. 1c). The raw CAT data was acquired in 5-min intervals and directly used in a point-by-point tidal harmonic analysis (Pawlowicz et al., 2002) that involves 5 tidal constituents (O_1, K_1, M_2, S_2 and MSF) and a the temporal mean of the residual current.

Fig. 6 presents tidal ellipse spatial distributions of tidal constituents O_1, K_1, M_2, S_2 and MSF (Fig. 6a–e), as well as the temporal mean of the residual current (Fig. 6g). The diurnal tidal constituent O_1 (Fig. 6a) is the greatest among the five tidal constituents, while the MSF (Fig. 6e) is the smallest among them. The spatially averaged amplitudes and standard deviations (i.e., spatial variation) of
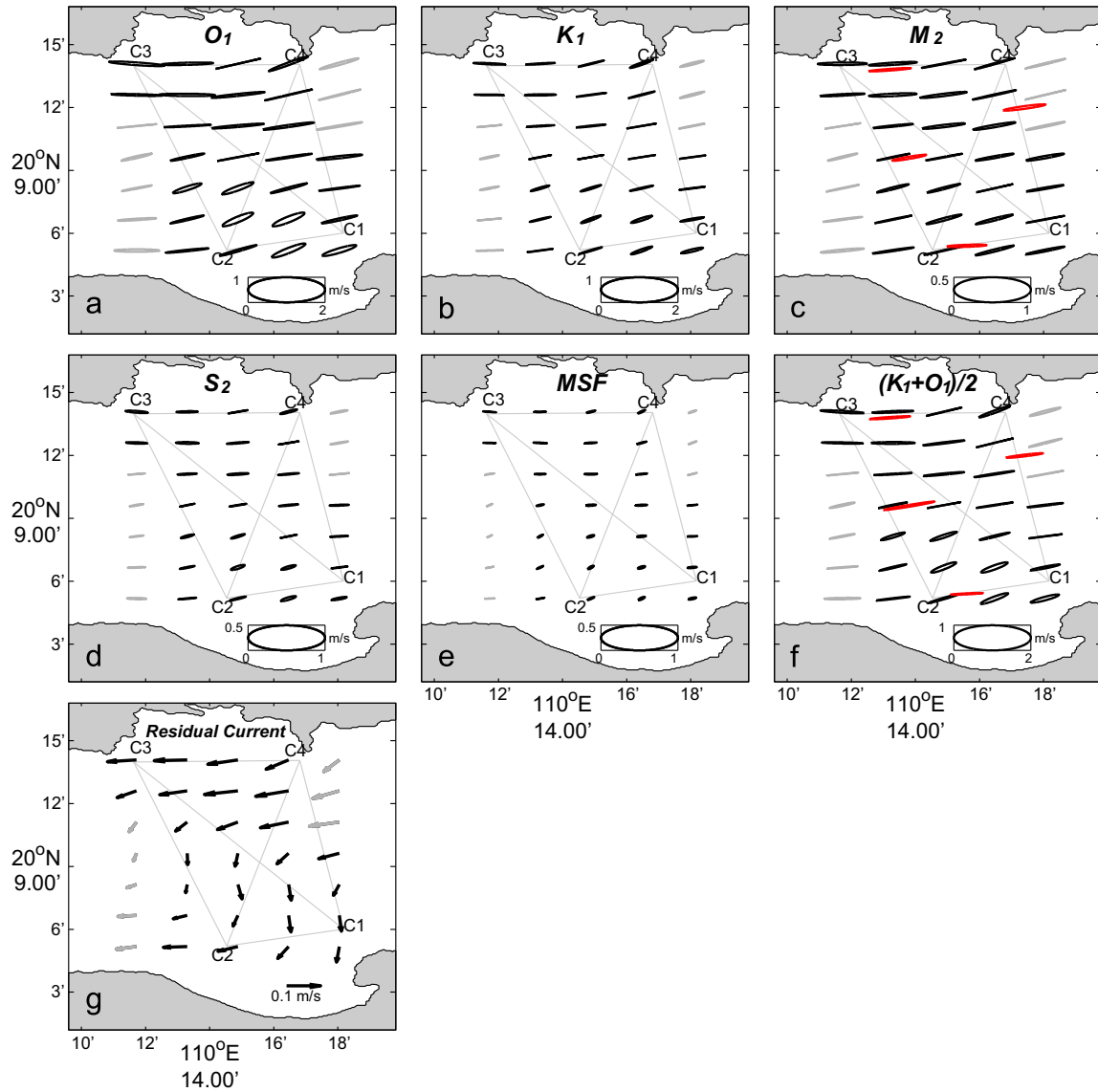
Fig. 6. Depth-averaged tidal current ellipses for the tidal constituents. (a) O_1, (b) K_1, (c) M_2, (d) S_2, (e) MSF and (f) diurnal $((K_1+O_1)/2)$, and (g) the temporal mean of residual current. The red tidal current ellipses in (c) and (f) are from Shi et al. (2002). Note that the length scale for the diurnal tidal current ellipses is different from the others. (For interpretation of the references to color in this figure legend, the reader is referred to the web version of this article.)

O_1, K_1, M_2, S_2 and MSF tidal constituents are summarized in Table 1. The spatially averaged amplitudes of O_1, K_1, M_2, S_2 and MSF follow the proportions 1.00:0.60:0.47:0.21:0.11. The major axis directions (anticlockwise from due east) of the tidal ellipses for the five constituents are generally along the strait direction of 8° (Table 1). The ellipticities, or ratios of minor axis to the major axis, of the five tidal constituents were generally small, ranging from 0.06 to 0.18, indicating that all tidal currents flowed dominantly along the strait. The temporal mean of the residual current was larger in the northern area than in the southern area; the spatially averaged westward speed was 7.3 ± 1.7 cm s^{-1} and the spatially averaged direction (anticlockwise from the east) was 227.3 ± 34.7° (Fig. 6g). The maximum temporal mean of the westward residual current speed was 12.4 cm s^{-1} in the northern QS.

In order to examine spatial structure variation of the residual currents during the experiment period, the residual current distributions were averaged over each diurnal cycle and plotted in Fig. 7. The residual currents changed in the magnitudes and directions. The residual currents were small when the diurnal tide dominated but large when the semidiurnal tide increased (after

Table 1
Spatially-averaged amplitude, direction (rotating anticlockwise from the east), errors of the major and minor axis lengths and their standard deviations for the O_1, K_1, M_2, S_2 and MSF tidal current constituents.

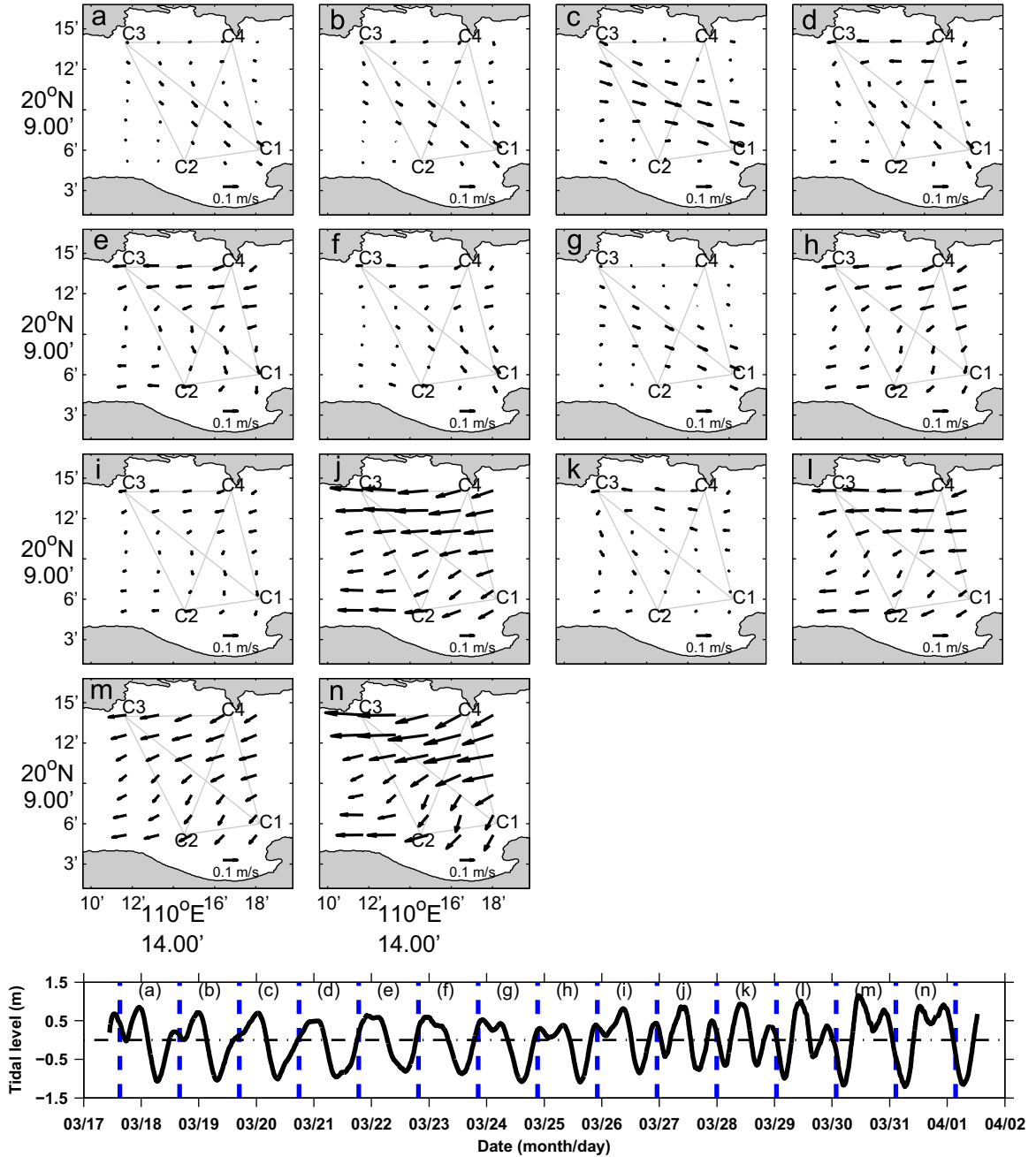| Tidal constituents	Amplitudes ± STDs (cm s^{-1})	Direction ± STDs (deg)	Errors of major axis length ± STDs (cm s^{-1})	Errors of minor axis length ± STDs (cm s^{-1})
O_1	57.5 ± 9.2	16.7 ± 10.0	7.4 ± 1.9	3.4 ± 1.3
K_1	34.3 ± 4.1	16.1 ± 8.6	7.0 ± 1.6	3.3 ± 1.2
M_2	27.0 ± 2.6	15.1 ± 6.0	3.6 ± 0.9	2.0 ± 0.7
S_2	12.0 ± 1.7	12.8 ± 8.2	3.8 ± 0.9	2.0 ± 0.8
MSF	6.6 ± 1.2	15.8 ± 13.5	6.0 ± 1.5	2.8 ± 1.0

Fig. 7. Vector plots of the residual current distributions averaged during each diurnal cycle. (a)–(n) Distributions corresponding to the cycles separated by blue broken lines in the bottom panel, where the tidal gauge data are also plotted with the black line.

March 25), consistent with mean residual transport trends (shaded horizontal bars in Fig. 4h). The time series of the spatial mean residual current averaged in the tomography domain (red line in Fig. 4h) also agreed well with residual transport (black line in Fig. 4h), verifying the inverse calculation.

3.4. CAT compared with shipboard ADCP

The tidal current velocity data obtained from inverse analysis of CAT data were interpolated to the shipboard ADCP track and then validated by the shipboard ADCP data. The current velocities obtained by the CAT measurements agreed well with the depth-averaged shipboard ADCP data, with 0.094 m s^{-1} and 0.066 m s^{-1} RSMDs, and correlation coefficients $r^2 = 0.980$, 0.847 for the along- and cross-strait velocity components, respectively (Fig. 8).

3.5. Error evaluation

We estimated the five major tidal current constituents from CAT data using inverse analysis. The CAT measurement error, inverse error, or non-tidal energy can influence the results of the tidal current constituents and non-tidal current. Here, we consider the 'error of tidal currents' to be the velocity signal not attributable to the tidal constituents and calculated as in Pawlowicz et al. (2002):

$$\sigma_{\xi} = \sqrt{\left(\frac{\partial F}{\partial A_r}\right)^2 \sigma_{A_r}^2 + \left(\frac{\partial F}{\partial A_i}\right)^2 \sigma_{A_i}^2 + \left(\frac{\partial F}{\partial B_r}\right)^2 \sigma_{B_r}^2 + \left(\frac{\partial F}{\partial B_i}\right)^2 \sigma_{B_i}^2},$$

(7)

where F is a non-linear function of A_k, B_k, i.e., $\xi = F(A_k, B_k)$, whose partial derivatives with respect to A_r, A_i, B_r, B_i can be determined exactly (Pawlowicz et al., 2002). $A_k = A_r + iA_i$, $B_k = B_r + iB_i$ are
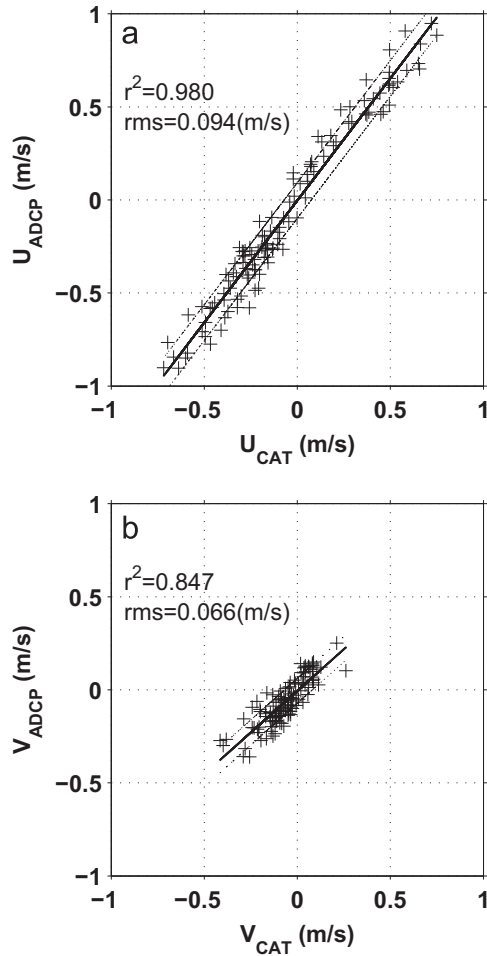
Fig. 8. Scatter plots of the velocity. (a) Along- and (b) across-strait components obtained between the shipboard ADCP data (V_{ADCP}) and the inversion results using CAT data (V_{CAT}). The solid line indicates the regression line derived from the least squares method. The two gray broken lines indicate the standard deviation of the difference.

harmonic constants of tidal constituent k. The subscripts r and i denote the real and imaginary parts. $\sigma_{A_r}^2$, $\sigma_{A_i}^2$, $\sigma_{B_r}^2$, $\sigma_{B_i}^2$ are the total residual powers for A_r, A_i, B_r, B_i, respectively.

The 'error of residual currents', not included in the tidal harmonic analysis, for a mean residual current is

$$\sqrt{\frac{\sum_{m=1}^{N}\left(v_0(t_m) - \overline{v_{0(t_m)}}\right)^2}{N-1}}, \tag{8}$$

where v_0 is the time dependent residual current, m denotes the time series sequence number and N denotes the time series length. $\overline{v_{0(m)}}$ denotes the temporal mean of the residual current. The 'error of tidal currents' in Eq. (7) and 'error of residual currents' in Eq. (8) were calculated using T_Tide Matlab software.

The error of the depth-averaged tidal currents along the major and minor axes of the five tidal constituent tidal ellipses and the residual current velocity are shown in Fig. 9. The error of the depth-averaged tidal currents was larger in the northern area than in the southern area. The error of the major axis length was also larger than the error of the minor axis length. The area mean (i.e., average over the tomography domain) errors and standard deviations of the O_1, K_1, M_2, S_2 and MSF tidal current constituents major and minor axes lengths are summarized in Table 1. The errors of the major axis lengths of the O_1, K_1, M_2, S_2 and MSF tidal current constituents was approximately 13%, 20%, 13%, 31% and

91%, respectively.

The errors of the residual current velocities were generally small, with somewhat larger values in the northern area than in the southern area (Fig. 9f). The maximum error of the residual current velocity was 2.1 cm s^{-1}, appearing at the northern part of the QS. The area mean of error for the residual currents is 1.2 cm s^{-}, which is approximately 17 % of the temporal mean of the residual currents.

4. Discussion

4.1. Comparisons with previous studies

To evaluate the accuracy of our estimated tidal currents, we compared our results with previous independent measurements. Estimated tidal current data from this study agreed well with results reported by Shi et al. (2002). They collected all available current data from observations in the QS from 1963 to 1999, which included the four data sites covered by our CAT observations. The diurnal (($O_1 + K_1$)/2) and semidiurnal tidal currents estimated from our CAT data (black ellipses) are consistent with those reported by Shi at al. (2002) (red ellipses) (Fig. 6c and f). The RMSD of the major axes, minor axes and diurnal tidal current ellipses orientations at the four sites are 14.3 cm s^{-1}, 4.0 cm s^{-1} and 12.3°, respectively; the RMSD of the major axes, minor axes and semidiurnal tidal current ellipses orientations at the four sites are 1.8 cm s^{-1}, 2.8 cm s^{-1} and 9.6°, respectively.

Shi et al. (2002) showed that mean residual currents in the QS during spring were stronger in the northern strait than in the southern strait (Fig. 8 in their paper). Using a three-dimensional numerical model, Chen et al. (2009) showed that the residual currents in the QS ranged between 3 and 30 cm s^{-1}, were stronger in the northern strait than in the southern strait, and were directed west in the northern area but south in the southern area (Fig. 8b1–b3 in their paper). Our results (Fig. 6g) show the same spatial variation between the northern area and the southern area as found previously, and residual current magnitudes that fell within the range of the model results. These comparisons affirm the validity of our method of estimating tidal currents by inversion analysis of CAT data.

Based on different observations, i.e., non-synchronous data, the volume transport due to residual currents in the QS have been estimated as 0.2–0.4 Sv in winter and spring (Shi et al., 2002), 0.055 Sv (Chen et al., 2007), 0.020–0.048 Sv (Yan et al., 2008), and 0.065 Sv (Zhu et al., 2014). Although these estimates vary in magnitude, they are consistently directed westward. Based on synchronous data and realistic bathymetry, we estimate a 0.044 Sv westward volume transport due to residual current in the spring, within the range of previously reported values.

4.2. Dynamics of residual currents

In a simulation of the QS including only tidal current forcing, a westward residual current was produced by tidal rectification (Shi et al., 2002). Inclusion of more forcing, such as winds, buoyant flux, and boundary currents in a tide-resolving model indicated that the sea level difference between the two entrances of the QS also significantly drives a throughflow in the QS (Gao et al., 2013). The spatial distributions of tidal currents given by our CAT data allow us to examine the possible factors controlling the residual currents in the QS.

By integrating the 3-dimensional momentum equations from the sea bottom up to the sea surface, we obtained the depth-averaged momentum equations in the across-strait direction
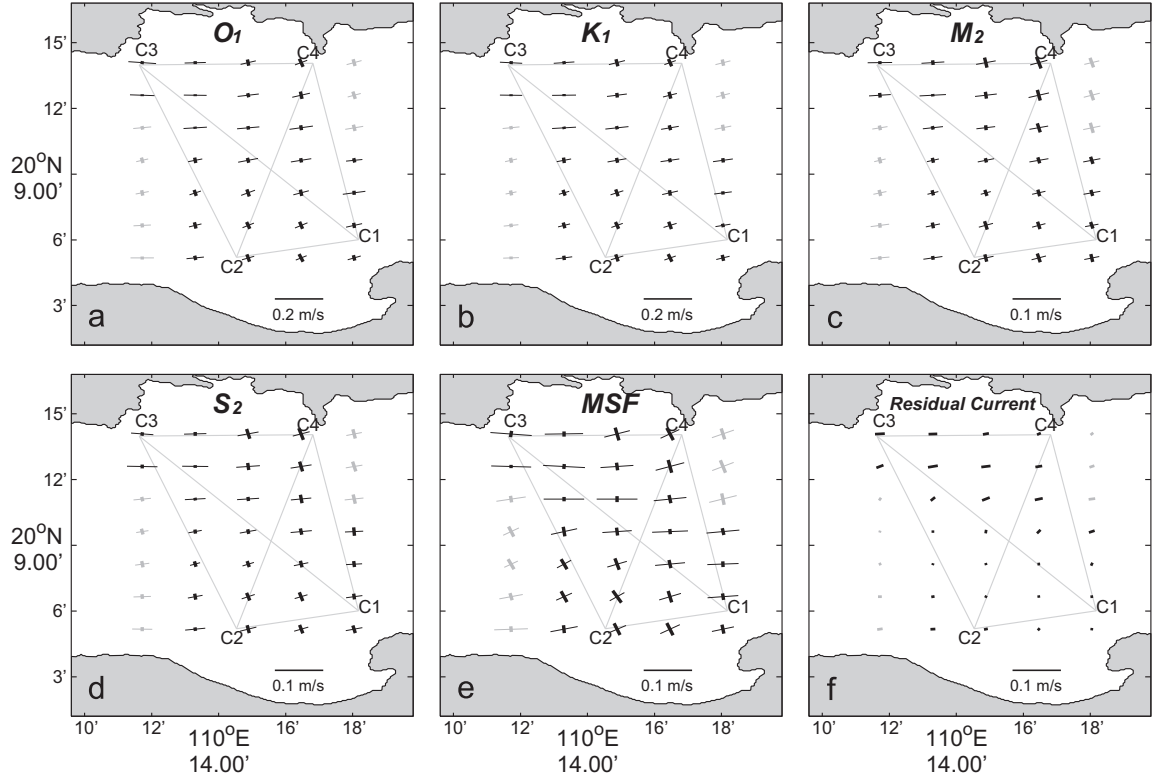
Fig. 9. Error of the five tidal constituents. The thin and thick lines indicate the error in the major and minor axes, respectively. Note that the length scale for the diurnal tidal current ellipses is different from the others.

$$\overline{u(\partial v/\partial x)} + \overline{v(\partial v/\partial y)} + \overline{fu}$$
$$= -\overline{g(\partial \eta/\partial y)} + \overline{A_h(\partial^2 v/\partial x^2)} + \overline{A_h(\partial^2 v/\partial y^2)}$$
$$- \overline{\tau_{by}/\rho h} + \overline{\tau_{wy}/\rho h},$$ (9)

and in the along-strait direction:

$$\overline{u(\partial u/\partial x)} + \overline{v(\partial u/\partial y)} - \overline{fv}$$
$$= -\overline{g(\partial \eta/\partial x)} + \overline{A_h(\partial^2 u/\partial x^2)} + \overline{A_h(\partial^2 u/\partial y^2)} - \overline{\tau_{bx}/\rho h} + \overline{\tau_{wx}/\rho h}$$ (10)

Here, u and v are the depth-averaged total currents given by CAT in the along-strait (x axis) and across-strait (y axis) directions, respectively; τ_{bx} and τ_{by} are the bottom friction in the along-strait and across-strait directions, respectively; τ_{wx} and τ_{wy} are the wind stresses in the along-strait and across-strait directions, respectively; f is Coriolis parameter; ρ is the water density (1022 kg m^{-3}); g is the acceleration of gravity; η is the elevation from the mean sea surface; A_h is the horizontal eddy viscosity coefficient; h is the water depth. Bars over each term denote temporal averages over 15 diurnal tidal cycles. The temporal variations of $\bar{u}$ and $\bar{v}$ are assumed to be negligible to the other terms in Eqs. (9) and (10).

The first two terms on the left hand sides of Eqs. (9) and (10) denote the nonlinear effects of tidal and residual currents that cause tidal rectification (T_{adv}); the third term on the left hand side is the Coriolis term (T_{cor}); the first term on the right hand side of Eq. (9) is the water elevation gradient in the across-strait direction; the first term on the right hand side of Eq. (10) is the water elevation gradient in the along-strait direction, partly corresponding to the sea levels at the two entrances of the QS; the second and third terms on the right hand side of the two equations are horizontal mixing (T_{hor}); the fourth and fifth terms on the right hand side of the two equations are the bottom friction (T_{bf}) and wind stresses (T_{wf}). We calculated the bold font terms shown in Eqs. (9) and (10) using our

data. In these calculations, the Coriolis parameter f was 5.0×10^{-5} s^{-1}, corresponding to the latitude of the QS, and the horizontal eddy viscosity coefficient (A_h) was 90 m^2 s^{-1}, as used by Cáceres et al. (2003). The bottom stresses were calculated as $\tau_{bx} = \rho C_d \sqrt{u^2 + v^2} u$ and $\tau_{by} = \rho C_d \sqrt{u^2 + v^2} v$, where C_d is 0.0025. The wind stresses were calculated as $\tau_{wx} = C_w \rho_a \sqrt{u_{wind}^2 + v_{wind}^2} u_{wind}$ and $\tau_{wy} = C_w \rho_a \sqrt{u_{wind}^2 + v_{wind}^2} v_{wind}$; C_w denotes the drag coefficient of the wind speed given by $C_w = 10^{-3} \times (0.63 + 0.066 \times \sqrt{u_{wind}^2 + v_{wind}^2})$; $\rho_a = 1.29$ kg m^{-3} is air density (Smith and Banke, 1975). u_{wind} and v_{wind} denote the eastward and northward wind velocity components from reanalysis of data with six hour intervals (http://apps.ecmwf.int/datasets/data/interim-full-daily/).

In the across-strait direction (Fig. 10), $\overline{u(\partial v/\partial x)}$ (Fig. 10a) was the largest and $\overline{\tau_{by}/\rho h}$ the smallest component (Fig. 10f). $\overline{v(\partial v/\partial y)}$ (Fig. 10b) was of the same order as T_{cor} (Fig. 10c) and T_{hor} (Fig. 10d and e). The area mean of the absolute values of T_{Cor}, T_{adv} ($\overline{u(\partial v/\partial x)} + \overline{v(\partial v/\partial y)}$), T_{hor} ($\overline{A_h(\partial^2 v/\partial x^2)} + \overline{A_h(\partial^2 v/\partial y^2)}$), T_{bf} and T_{wf} were (2.42, 8.67(7.02+1.65), 6.03(2.89+3.14), 0.85 and 0.30) ($\times 10^{-6}$ m s^{-2}), respectively. Then, the approximate ratios of these terms were $T_{Cor}:T_{adv}:T_{hor}:T_{bf}:T_{wf} = 1.00:3.58:2.50:0.35:0.12$. T_{bf} and T_{wf} were negligible in the across-strait direction momentum balance. The water elevation gradient was approximately 4.3×10^{-6} m s^{-2} by Eq. (9). Using the width of the QS (19.5 km), this value corresponded to a sea level difference of 0.009 m across the strait, close to 0.01 m reported by Shi et al. (2002). Apparently, the geostrophic balance does not hold exactly for the residual current in the along-strait direction because of large nonlinear effect contributions (T_{adv}) and frictional forcing due to horizontal shear (T_{hor}). In other words, our synchronous data supported tide-induced residual currents, as suggested earlier by non-synchronous data (Shi et al., 2002).
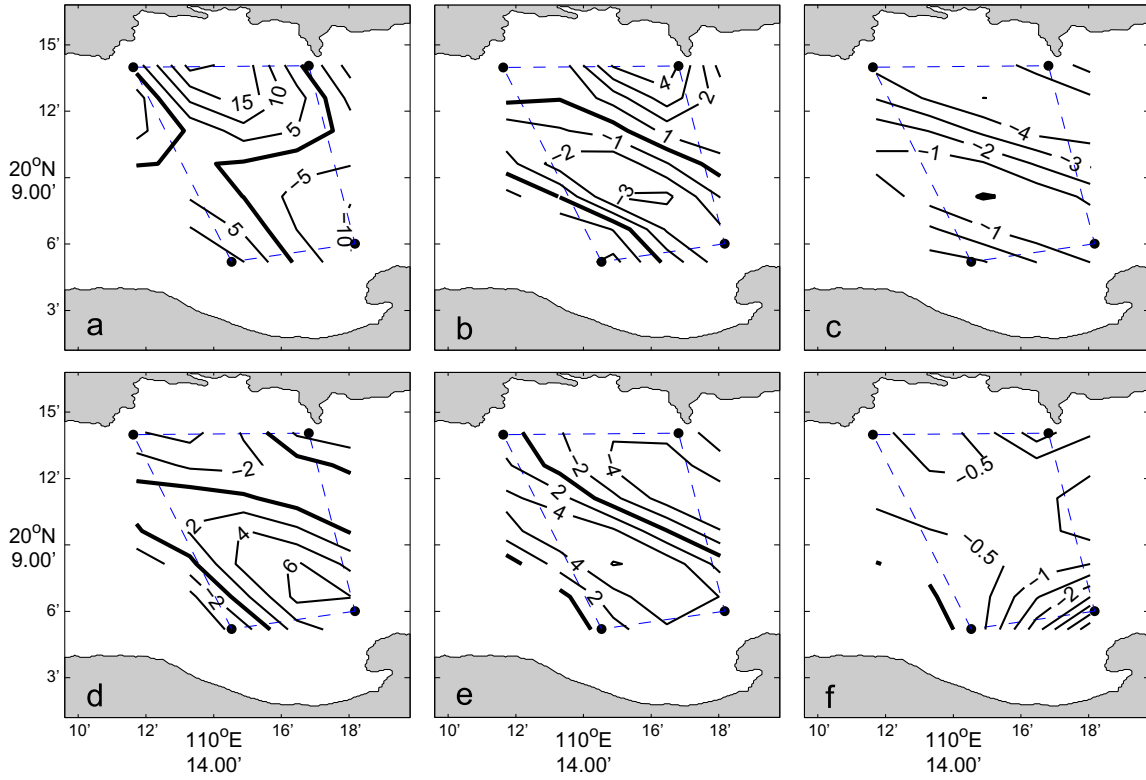
Fig. 10. Contour plots for the terms in Eq. (5). (a) $\overline{u(\partial v/\partial x)}$, (b) $\overline{v(\partial v/\partial y)}$, (c) $\overline{fu}$, (d) $\overline{A_h(\partial^2 v/\partial x^2)}$, (e) $\overline{A_h(\partial^2 v/\partial y^2)}$ and (f) $\overline{\tau_{by}/\rho h}$. The units in all panels is 10^{-6} m s^{-2}.

In the along-strait direction (Fig. 11), the T_{adv} of $\overline{u(\partial u/\partial x)}$ (Fig. 11a) was the largest and the T_{Cor} is the smallest (Fig. 11c). The area mean for the absolute values of the T_{Cor}, T_{adv} ($\overline{u(\partial u/\partial x)} + \overline{v(\partial u/\partial y)}$), T_{hor} ($\overline{A_h(\partial^2 u/\partial x^2)} + \overline{A_h(\partial^2 u/\partial y^2)}$), T_{bf} and T_{wf} were [1.70, 7.88 (5.50+2.38), 6.03 (2.07+3.96), 2.27 and 0.33]

($\times 10^{-6}$ m s^{-2}), respectively. The approximate ratios of these terms were $T_{Cor}:T_{adv}:T_{hor}:T_{bf}:T_{wf}$ = 1.00:4.63:3.55:1.34:0.19. The T_{wf} was negligible in the along-strait direction momentum balance. Eq. (10) estimated the water elevation gradient to be approximately 2.2×10^{-6} m s^{-2}, which corresponds to a sea level
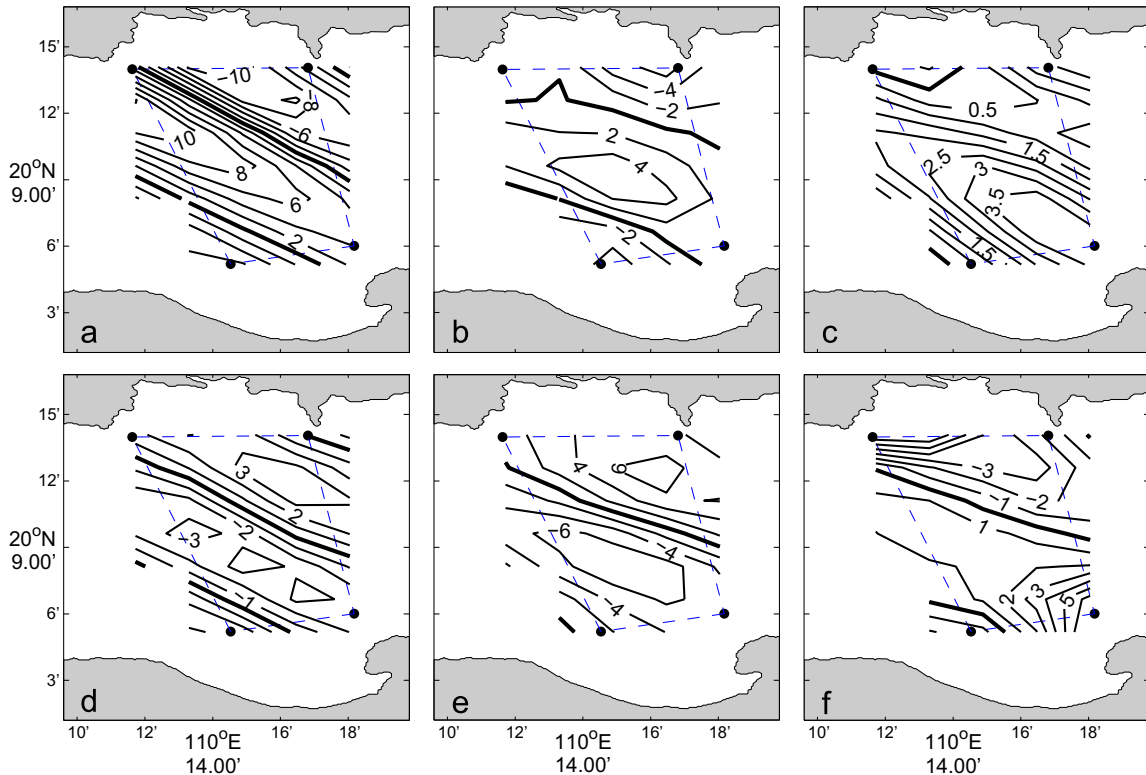

Fig. 11. Contour plots for the terms in Eq. (6). (a) $\overline{u(\partial u/\partial x)}$, (b) $\overline{v(\partial u/\partial y)}$, (c) $\overline{fv}$, (d) $\overline{A_h(\partial^2 u/\partial x^2)}$, (e) $\overline{A_h(\partial^2 u/\partial y^2)}$ and (f) $\overline{\tau_{bx}/\rho h}$. The unit in all panels is 10^{-6} m s^{-2}.

difference of 0.015 m, using the length of the QS (70 km). A negative (westward) along-strait water elevation gradient balancing momentum in the along-strait direction implies that tidal rectification (Shi et al., 2002) is not the sole mechanism of westward residual current formation in the QS. The sea level difference between the two entrances of the QS also importantly affects westward residual current formation in the QS (Gao et al., 2013).

5. Conclusions

We present the first synchronous observations of tidal current, residual current, and volume transport in the QS. A 15-day coastal acoustic tomography experiment measured the tidal currents in the QS using four acoustic stations during March, 2013. Throughout the experiment, reciprocal sound transmissions were performed along six transmission lines. Shipboard ADCP surveys performed along the sound transmission lines provided independent transport estimates and comparisons with the CAT data.

The range-averaged along-transect current velocities estimated using differential travel time data ($\Delta\tau$) agreed well with ADCP measurements. The differential travel time data correlate well with volume transport (Q_{ADCP}) through the QS estimated from the ADCP data. The Q_{CAT} for the entire CAT experiment period, predicted using the empirical regression formula between Q_{ADCP} and $\Delta\tau$, ranges from -0.710 to 0.859 Sv, with a 0.044 Sv mean westward volume transport of residual (time independent) current.

Inverse analysis was adopted to reconstruct tidal current distributions from $\Delta\tau$ obtained between paired CAT stations. Using the current data from inverse analysis, we obtained harmonic constants of five major tidal currents (K_1, O_1, M_2, S_2, and MSF), and the residual current in the QS. The major axes of the tidal ellipses of the five constituents were generally directed along the strait. The ratios of O_1, K_1, M_2, S_2 and MSF tidal currents amplitudes were 1.00:0.60:0.47:0.21:0.11. The residual current flowed westward, stronger in northern area than in southern area and turned from a westward direction in the northern area to southward in southern area of the strait.

The dynamic analysis based on the currents estimated from CAT data was used to examine the controlling factors of the residual currents in the QS. The residual current varies significantly during the 15 days, such that it is stronger in the period of coexistence of semi-diurnal and diurnal tides than in the period of diurnal tide. The westward residual current in the QS was caused by both tidal rectification and the sea level difference between its two entrances.

The volume transport of the residual current averaged over each diurnal tide period was small during the diurnal tide and became larger when the semidiurnal tide was dominant. This increase implies that the temporal variation of residual currents cannot be explained by tidal rectification alone, which usually gives a proportional relation between tidal current and residual current. Therefore, a long-term (>1 year) current monitoring the QS is necessary for a full understanding of the mechanisms controlling transport through the QS. The easy handling of the CAT system and its performance (as shown in this study) suggest that the CAT system is potentially a highly viable way to achieve this difficult goal.

References

Bao, X.W., Hou, Y.J., Chen, C.S., Chen, F., Shi, M.C., 2005. Analysis of characteristics and mechanism of current system on the west coast of Guangdong of China in summer. Acta Oceanol. Sin. 24 (4), 1–9.

Ca´ceres, M., Valle-Levinson, A., Atkinson, L., 2003. Observations of cross-channel structure of flow in an energetic tidal channel. J. Geophys. Res. 108 (C4), 3114. http://dx.doi.org/10.1029/2001JC000968.

Chen, B., Yan, J.H., Wang, D.R., Shi, M.C., 2007. The transport volume of water through the Qiongzhou Strait in the winter season. Period. Ocean Univ. China 37 (3), 357–364 (in Chinese with English abstract).

Chen, C.L., Li, P.L., Shi, M.C., Zuo, J.C., Chen, M.X., Sun, H.P., 2009. Numerical study of the tides and residual currents in the Qiongzhou Strait. Chin. J. Oceanol. Limnol. 27 (4), 931–942.

Chen, D.S., Chen, B., Yan, J.H., Xu, H.F., 2006. The seasonal variation characteristics of residual currents in the Qiongzhou Strait. Trans. Oceanol. Limnol. 2, 12–17 (in Chinese with English abstract).

Gao, J., Xue, H., Chai, F., Shi, M., 2013. Modeling the circulation in the Gulf of Tonkin, South China Sea. Ocean Dyn. 63, 979–993. http://dx.doi.org/10.1007/s10236-013-0636-y.

Gordon, R.L., 1989. Acoustic measurement of river discharge. J. Hydrau. Eng. 115 (7), 925–936.

Kaneko, A., Yamaguichi, K., Yamamoto, T., Gohda, N., Zheng, H., Fadli, S., Lin, J., Nguyen, H.Q., 2005. Coastal acoustic tomography experiment in the Tokyo Bay. Acta Oceanol. Sin. 24, 86–94.

Kaneko, A., Mizuno, S., Koterayama, W., Gordon, R.L., 1992. Cross-stream velocity structures and their variation of Kuroshio around Japan. Deep-Sea Res. 39, 1583–1594.

Pawlowicz, R., Beardsley, B., Lentz, S., 2002. Classical tidal harmonic analysis including error estimates in MATLAB using T_TIDE. Comput. Geosci. 28, 929–937.

Munk, W., Worcestor, P.F., Wunsch, C., 1995. Ocean Acoustic Tomography. Cambridge Univeristy Press, Cambridge.

Park, J.H., Kaneko, A., 2001. Computer simulation of the coastal acoustic tomography by a two-dimensional vortex model. J. Oceanogr. 57, 593–602.

Shi, M.C., Chen, C.S., Xu, Q.C., Lin, H., Liu, G., Wang, H., Wang, F., Yan, J., 2002. The role of Qiongzhou Strait in the seasonal variation of the South China Sea circulation. J. Phys. Oceanogr. 32 (1), 103–121.

Smith, S.D., Banke, E.G., 1975. Variation of the sea surface drag coefficient with wind speed. Q. J. R. Meteorol. Soc. 101, 665–673.

Teledyne RD Instruments, 2013. A Teledyne RD Instruments Datasheet. ⟨www.rdinstruments.com⟩, 2.

Wang, D., Hong, B., Gan, J., Xu, H., 2010. Numerical investigation on propulsion of the counter-wind current in the northern South China Sea in winter. Deep-Sea Res. 57, 1206–1221.

Wu, D.X., Wang, Y., Lin, X.P., Yang, J.Y., 2008. On the mechanism of the cyclonic circulation in the Gulf of Tonkin in the summer. J. Geophys. Res. 113, C09029. http://dx.doi.org/10.1029/2007JC004208.

Yamaguchi, K., Lin, J., Kaneko, A., Yamamoto, T., Gohda, N., Nguyen, H.-Q., Zheng, H., 2005. A continuous mapping of tidal current structures in the Kanmon Strait. J. Oceanogr. 61, 283–294.

Yan, C., Chen, B., Yang, S., Yan, J., 2008. The transportation volume of water through the Qiongzhou Strait in winter season. Trans. Oceanol. Limnol. 1, 1–9.

Yang, S.Y., Bao, X.W., Chen, C.S., Chen, F., 2003. Analysis on characteristics and mechanism of current system in west coast of Guangdong Province in the summer. Acta Oceanol. Sin. 25, 1–8 (in Chinese with English abstract).

Zhu, X.-H., Ma, Y.-L., Guo, X., Fan, X., Long, Y., Yuan, Y., Xuan, J.-L., Huang, D., 2014. Tidal and residual currents in the Qiongzhou Strait estimated from shipboard ADCP data using a modified tidal harmonic analysis method. J. Geophys. Res. Oceans 119, 8039–8060. http://dx.doi.org/10.1002/ 2014JC009855.